Progress in Additive Manufacturing (2026) 11:4477–4495
https://doi.org/10.1007/s40964-026-01600-3

RESEARCH

Experimental analysis of the powder flow in a continuous coaxial nozzle for laser metal deposition

Lorenzo Pedrolli[1] · Jon Iñaki Arrizubieta Arrate[2] · Giulio Bonifazi[1] · Aitzol Lamikiz[2] · Beatriz Achiaga[1] · Alejandro Lopez[1]

Received: 4 November 2025 / Accepted: 15 February 2026 / Published online: 11 March 2026

Abstract

This work presents an experimental analysis of the powder flow from a continuous coaxial nozzle for Laser Metal Deposition (LMD), demonstrating the ability to identify the transients and high-speed process flow dynamics. High-speed video tracking of individual particles enabled detailed analysis of size, spatial distribution, and velocities, revealing significant flowrate variations over time of up to 20%, which may compromise deposition quality. These oscillations emerge from the large number of interactions among particles, carrier gas, and nozzle walls, reflecting complex, self-excited flow dynamics not captured by time-averaged measurements. The standoff distance, defined as the optimal distance between the nozzle and the workpiece, was determined with unprecedented temporal resolution. In the most representative case, the average standoff distance was found to be approximately $16.0\ \mathrm{mm}$, with oscillations over time of up to 19%, due to variations in both particle trajectories and quantity over time. The particle size distribution was consistent with the manufacturer's specifications, a good indication of the method's accuracy, and an error estimation is performed to determine the expected precision of the measurements. A key aspect of this work, and its main contribution, is the development of a workflow capable of tracking individual particles to determine the instantaneous powder mass flowrate, providing a reliable approach to monitor and optimize powder delivery in the LMD process.

Keywords Directed energy deposition (DED) · Laser metal deposition (LMD) · Powder delivery · High-speed imaging · Particle tracking · Standoff distance · Flow characterization

1 Introduction

Directed Energy Deposition (DED) processes are a key subset within the realm of AM technology. DED is a category of additive manufacturing that leverages various energy sources, such as lasers or electron beams, to precisely bond material onto a substrate, forming intricate 3D structures. This technology is gaining traction in the world of multi-material and hybrid manufacturing. By combining different materials and deposition techniques, DED processes can produce components with tailored material properties, offering a level of customization and performance that traditional manufacturing methods struggle to match. In Laser Metal Deposition (LMD), the material is added in powder form and locally heated using a laser source to melt it onto the substrate.

The shielding and carrier gas used in most cases is Argon, which protects both the powder and the melt pool from oxidation. The whole powder delivery system is a continuous

✉ Lorenzo Pedrolli
l.pedrolli@deusto.es

✉ Alejandro Lopez
alejandro.lopez@deusto.es

Jon Iñaki Arrizubieta Arrate
joninaki.arrizubieta@ehu.eus

Giulio Bonifazi
g.bonifazi@deusto.es

Aitzol Lamikiz
aitzol.lamikiz@ehu.eus

Beatriz Achiaga
beatriz.achiaga@deusto.es

[1] Department of Mechanics, Design and Industrial Engineering, University of Deusto, Bilbao, Spain

[2] Department of Mechanical Engineering, University of the Basque Country, Leioa, Spain

loop until the nozzle, where the powder needs to transverse a short distance without being constrained by pipes and conducts. A proper flow of powder is critical for a uniform and stable deposition, and consequently for all the quality indicators of the finished or repaired part, and for the reduction of waste. In this case, waste would be defined as anything that increments the use of any resource. Examples can be the lost powder that didn't adhere to the melt pool, or the additional manufacturing steps required to obtain full functionality. The nozzle's setup, as a part of an LMD system, is crucial in ensuring the proper powder delivery to the melt pool. The metered stream of powder flows through a length of conveying system and reaches the deposition head, exiting through the nozzle. The deposition head is the defining system of the LMD technology, providing the laser power, shielding gas, and a constant stream of filler material in powder form.

The nozzle setup is a defining feature of LMD systems, providing laser power, shielding gas, and a constant stream of filler material. Observations from prior studies [1, 2] indicate that periodic flow variations at the nozzle exit can significantly affect deposition quality, leading to surface irregularities such as hills and valleys. Pneumatic powder feeders are commonly used for feedstock handling, delivering a uniform gas/powder mixture to the nozzle. Among various nozzle configurations, continuous coaxial and discrete coaxial setups are most commonly employed in LMD. Both configurations use a central laser beam to form the melt pool, with powder delivered at a converging angle.

Previous research has investigated the behavior of powder delivery systems in Laser Metal Deposition (LMD) processes. Tabernero et al. [3] conducted a detailed study on the continuous coaxial nozzle, focusing on the numerical simulation and experimental validation of powder flux distribution. They used one-way coupled particle tracking to simulate particle paths, verifying their findings by comparing the particle concentrations deposited in cylinders of various diameters at a known distance from the nozzle.

In another study, Ostolaza et al. [4] performed a Computational Fluid Dynamics (CFD) analysis on the continuous coaxial nozzle, as depicted in Fig. 2. Their research concluded that the $k-\omega$ SST turbulence model is most suitable for simulating the flow characteristics in this scenario. They emphasized the importance of accurately determining process parameters, especially when switching materials. The study compared simulation results with experimental data using long exposure images to map particle concentration, as shown in Fig. 1.

López-Martinez et al. [5] studied the powder catchment efficiency in continuous and discrete nozzles in inclined configurations, highlighting a deformed stream shape due to the effect of gravity and internal nozzle construction. Their study also considered a time-averaged information on the stream shape, captured using a long exposure of the image.

Additionally, Gao et al. [6] explored the dynamics of powder flow in LMD nozzles through both experimental and numerical methods. They highlighted how variations in nozzle design and process parameters significantly affect powder distribution and deposition efficiency. Their findings underscore the necessity of optimizing nozzle configurations to achieve uniform and efficient material deposition.

The review by Guner et al. [7], jointly with the one from Piscopo et al. [8] complete the picture, denoting a gap in the research related to the flow uniformity during the deposition.

Existing experimental studies determine the particle concentration on the focus spot using time-averaged data and long exposures. These methods do not provide much detail on the particle dynamics, such as their velocities and size

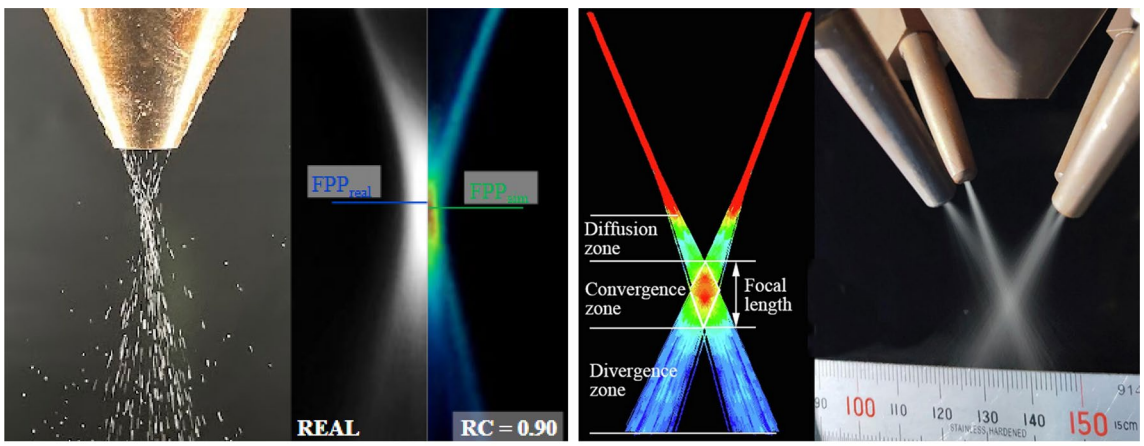

Fig. 1 **a** Comparison of simulated and experimental powder distribution morphology. Adapted from Ostolaza et al. [4], who uses the same continuous coaxial nozzle as Fig. 2. **b** Powder flow zones and focal length in a discrete coaxial nozzle, highlighting the diffusion, convergence, and divergence zones. Adapted from Gao et al. [6]

distributions, which are helpful for understanding the flow characteristics and optimizing the deposition process.

This work aims to fill this gap by providing a detailed experimental analysis of the evolution of powder flow in a continuous coaxial nozzle for LMD. The study employs high-speed video recordings to track individual particles, allowing for a comprehensive analysis of their size distribution, spatial distribution, and velocities. The results will be used to determine the standoff distance, defined as the optimal distance between the nozzle and the workpiece, and to assess the uniformity of the powder stream exiting the nozzle. The findings will contribute to a better understanding of powder flow dynamics in LMD processes and provide insights for optimizing deposition quality.

2 Materials and methods

This study focuses on analyzing the flow exiting the continuous coaxial nozzle, as illustrated in Fig. 2. Within it, the powder exits an annular slit surrounding the central orifice. This type of construction generates good and uniform results, not being affected by the (planar) direction of deposition. The nozzle contains an internal distributor structure to guide the powder.

Three main flowrates can be controlled in the experimental setup, as illustrated in the nozzle schematic (Fig. 3): the powder flowrate, the carrier gas flowrate, and the shielding gas flowrate. The powder flowrate refers to the mass of powder delivered per unit time, while the carrier and shielding gas flowrates correspond to the flow of Argon gas, each supplied from a separate flowmeter.

The experiment is run "cold," meaning that a nozzle was mounted on a stand outside the machine and operated without the laser, as represented in Fig. 3.

The experiments involved high-speed video recordings to capture the powder flow dynamics. The primary parameters varied in the experiments were the rotational speed percentage (RPM) of the powder feeder (which determines the powder flowrate in grams per minute), carrier gas flowrate, and shielding gas flowrate. These parameters were selected based on their significant impact on the powder flow characteristics and the overall quality of the deposition process.

The powder feeder is a Sultzer Metco Twin 10C powder feeder [9]. A rotating disk with an annular groove controls the flowrate, which is proportional to the disk's rotational speed. A spreader prevents overfilling, and the system's internal pressure pushes the powder through the outlet. The hopper is grounded to discharge static, a stirrer prevents powder arching, and the powder is pre-heated at $60°C$ to eliminate humidity.

2.1 Powder

The powder used in the experiments was Metco Additive 316 L, a gas-atomized stainless steel powder with a nominal particle size between $-106 + 45\ \mu\text{m}$. The material density is $\rho = 7.98\ \text{g/cm}^3$, and the chemical composition reported by the manufacturer [10]. The powder was stored in a dry environment to prevent moisture absorption, and handled

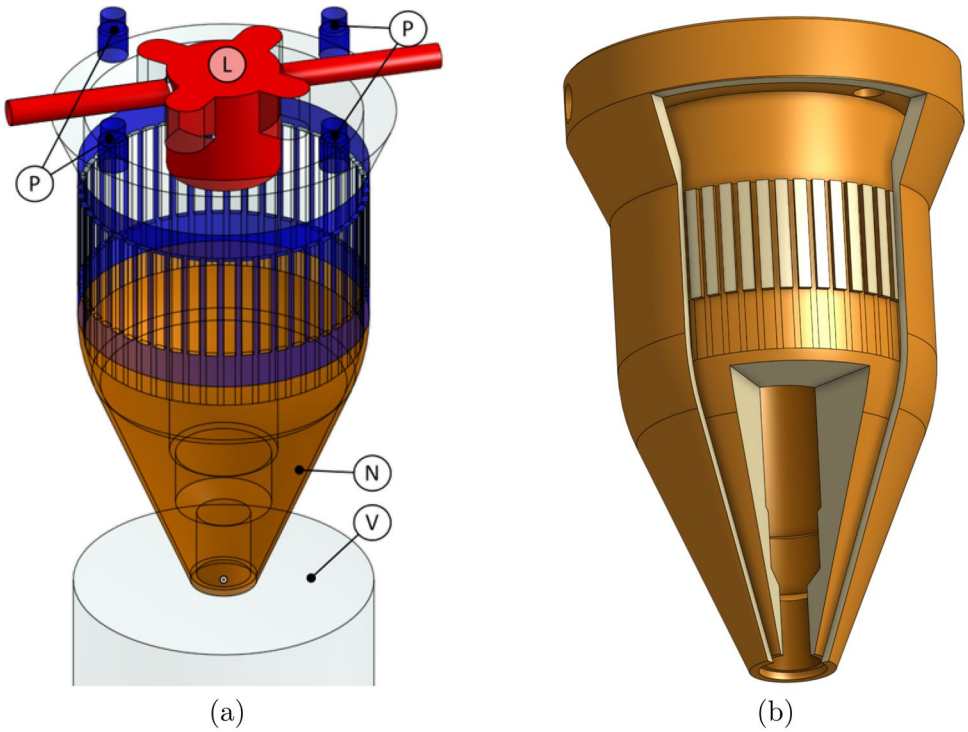

Fig. 2 3D CAD models of the nozzles analyzed in this work. The internal fluid domain is shown in (**a**), annotations indicate: the powder ports (Ⓟ), the laser and shielding gas port (Ⓛ), the nozzle body (Ⓝ), and the discharge volume (Ⓥ). **b** shows the sectioned view of the nozzle body

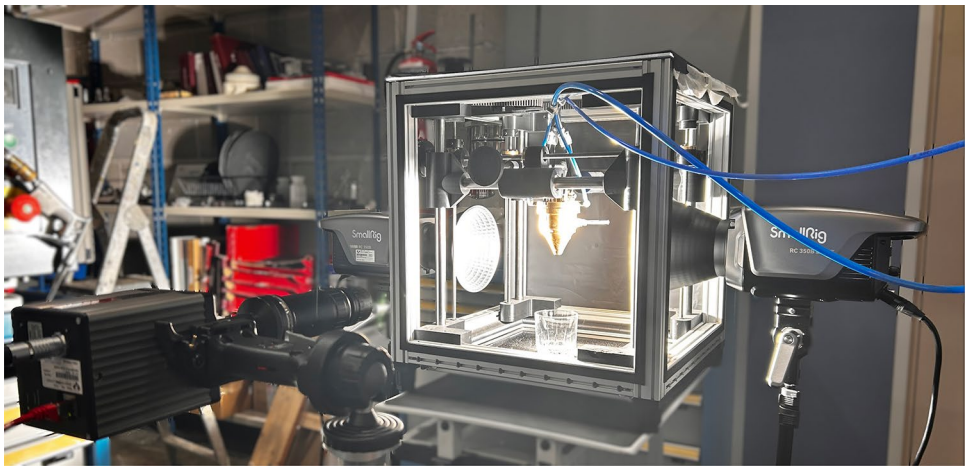

Fig. 3 Experimental setup for powder flow analysis in the LMD process, see Fig. 5**a**

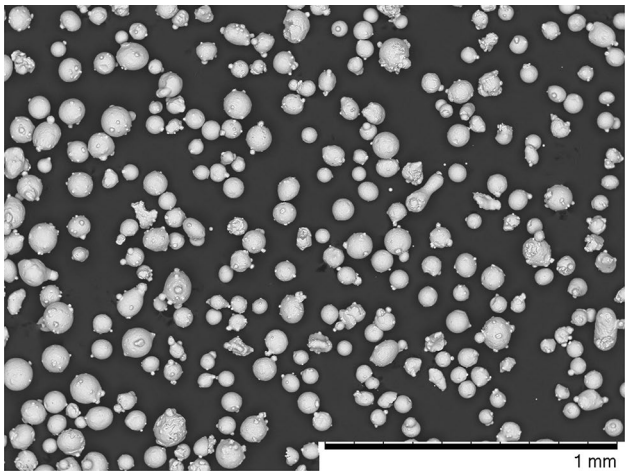

Fig. 4 Scanning electron microscopy (SEM) image of the metco additive 316 L powder used in the experiments. The nominal particle size is between $-106 + 45$ μm

Table 1 Process parameters and their values

	Parameter	Value 1	Value 2	Value 3
$\dot{m}_p$	Powder flow (g/min)	1.5	3.0	4.5
Q_c	Carrier gas flow rate (L/min)	2	3	5
Q_s	Shielding gas flow rate (L/min)	5	10	15

according to standard procedures to ensure consistent flow characteristics. The powder was characterized using Scanning Electron Microscopy (SEM) to verify its morphology, as shown in Fig. 4. The elasitc modulus of the powder is $E = 211$ GPa, with Poisson ratio $\nu = 0.3$. The average coefficient of restitution is $e = 0.64$ and the coefficient of sliding friction is $\mu = 0.5$ [11].

2.2 Experimental parameters and levels

The experimental matrix was designed using a Taguchi Orthogonal Array (L9) to systematically investigate the effects of these parameters with a minimal number of runs.

Table 2 Parameters and levels for the taguchi orthogonal array (L9) used in the experiment

Run	Powder flow (g/min)	Carrier gas (L/min)	Shielding gas (L/min)
1	1.5	2	5
2	1.5	3	10
3	1.5	5	15
4	4.5	2	10
5	4.5	3	15
6	4.5	5	5
7	3	2	15
8	3	3	5
9	3	5	10

The parameters and their corresponding levels used in the Taguchi array are listed in Table 1

The specific combinations of these levels for each experimental run are shown in Table 2.

2.3 Camera setup

High-speed videos were recorded using an AOS L-PRI camera equipped with a 100 mm c-mount lens. By cropping the sensor to a resolution of 844×1304 px, recordings were performed at 4490 fps, corresponding to a frame time of 0.2227 ms/frame. At a distance of 500 mm from the nozzle, the resulting field of view was 13.2×20.4 mm, with a pixel size of 15.6 μm.

Previous studies [3, 4, 6, 12, 13] commonly employed a side-illumination configuration, schematically shown in Fig. 5a. In this setup, flicker-free LED lights illuminate the particle stream from the sides against a black background, and particles are visualized through reflected light, producing bright spots as shown in Fig. 5c. While effective for qualitative visualization and long-exposure imaging, this configuration posed limitations for the present work: exposure times on the order of 90 μs led to motion streaks for fast-moving particles, and the recorded intensity strongly

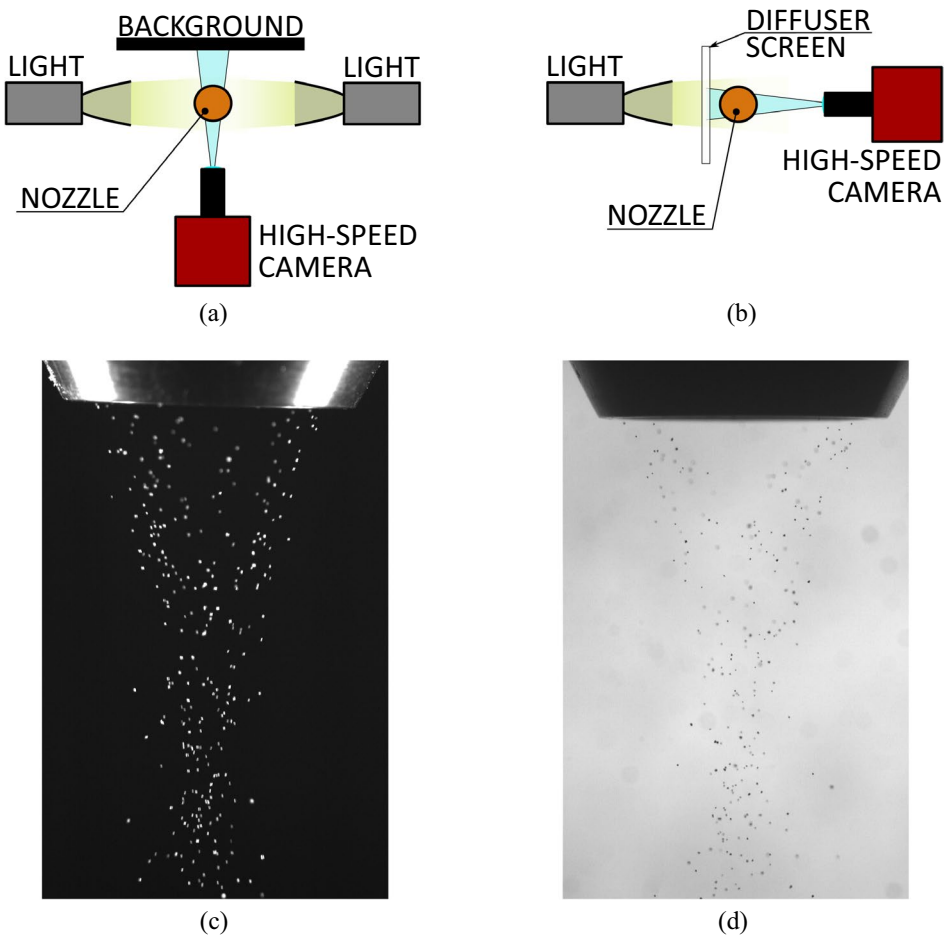

Fig. 5 Setup and raw results of the two camera configurations used in the experiment: **a** side illumination setup, **b** back illumination setup, **c** side illumination result (3530 fps, 3× gain, 90 μs exposure), **d** back illumination result (4490 fps, 3× gain, 16 μs exposure)

depended on particle shape and surface roughness, occasionally causing glare and sensor saturation.

To overcome these limitations, a back-illumination configuration was adopted in this study, as illustrated in Fig. 5b. A high-intensity LED spotlight, combined with a diffuser, was positioned behind the particle stream to generate a spatially uniform white background. In this configuration, particles appear as dark spots against the illuminated background, as shown in Fig. 5d. Their apparent size is determined primarily by the projected particle shadow rather than surface reflectivity, significantly reducing intensity variability and preventing sensor saturation.

The improved contrast enabled the use of shorter exposure times (16 μs), effectively eliminating motion-induced streaking and yielding sharper particle images. Moreover, the back-illumination approach provides a well-defined optical geometry that can be further enhanced through the use of telecentric optics, which would minimize perspective effects and geometric distortions.

2.4 Particle tracking

The videos recorded by the AOS camera were saved as `*.mp4` compressed videos and analyzed using the the image processing software Fiji/ImageJ [14]. This required the use of the additional FFMPEG library.

The sequence of images was then pre-processed using a script, which performs:

Calibration: The image stack is calibrated to reflect the physical dimensions of the system. The frame rate–and thus the time between frames–is known with high precision from the camera settings. The nozzle tip, whose diameter was measured beforehand, is visible within the frame. This known dimension was used to scale the image stack, allowing for accurate spatial calibration of the observed region.

Pre-processing: The image stack is first converted to an 8-bit grayscale format. A median projection along the stack is then computed to generate a background image, which is subsequently subtracted from the original stack. This step enhances the visibility of particles by removing static background noise and improving contrast.

Thresholding: The resulting image stack is converted to a binary mask.

The TrackMate plugin was used once again [15], with the code developed and reported in [16]. This allowed tracking of the rapid particle flow, as well as determining relevant metrics on the particle characteristics.

Ferreira et al. analyzed gas and powder streams using optical methods, such as laser sheets, to visualize the flow characteristics [17]. In contrast, the current study does not require laser sheets, as particle tracking provides a more granular and dynamic understanding by tracking individual particles. This approach allows for a more precise analysis of particle behavior and distribution, enhancing the overall understanding of the LMD process.

3 Results and discussion

The information coming from the Particle Tracking is analyzed, with the primary objective of observing the irregularity in the mass flowrate.

The tracked flow is exemplified in Fig. 6, which reports the tracks 10 frames backwards in time (panel a), and all the tracks superimposed (panel b). Each recording was approximately 0.07 s long, containing around $5\,000$ tracks, $100\,000$ edges, $125\,000$ spots (depending on the flowrate). Thanks to the good image quality, virtually all particles were recognized and tracked individually.

It was also observed from the identified spots that each frame contains an average of 416 particles. For further analysis, a 1 mm thick slice across the average standoff distance, determined in Sect. 3.2, contains $N = 17.5 \pm 6.5$ particles (mean ± standard deviation) at each frame. When considering a longer time window of 2 ms, or around 9 frames, this number increases proportionally to $N = 153.9 \pm 39.6$. This will become relevant when estimating the accuracy of the error of the proposed measurements, in Sect. 3.6.

3.1 Particle size distribution

Backside illumination allows particles to be observed without glare, enabling accurate size measurements. This technique was similarly employed by Nadimi et al. [18], who used multiple viewpoints to capture particle morphology comprehensively. As explained in Sect. 3.6, the particle size is determined from the covered area rather than a direct measurement of the diameter, resulting in an error that gets proportionally smaller for larger particles.

Figure 7 presents the cumulative Particle Size Distribution (PSD) by number, derived from nearly 70 000 particles tracked across all nine experimental cases (Table 2). Particle diameters are computed as the mean value along each trajectory. The mean PSD (solid blue line) and inter-case variability (shaded band, ± 1σ) demonstrate good repeatability across conditions. The uncertainty band represents a Type A evaluation following the Guide to the Expression of Uncertainty in Measurement (GUM) [19], quantifying measurement variability across the nine operating conditions. A Rosin-Rammler distribution (dashed red line) is fitted to the combined dataset, yielding characteristic parameters of $a = X$ μm and $n = Y$.

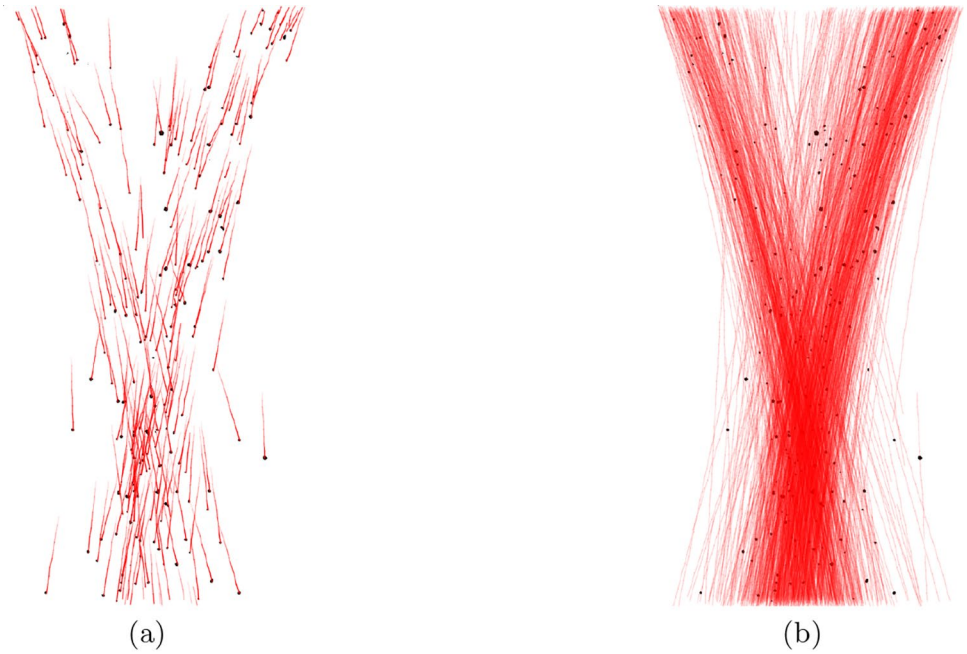

Fig. 6 Particle tracking results for case 5 in Table 2. **a** Tracks representing 10 timesteps backward in time. **b** All full-length recorded tracks

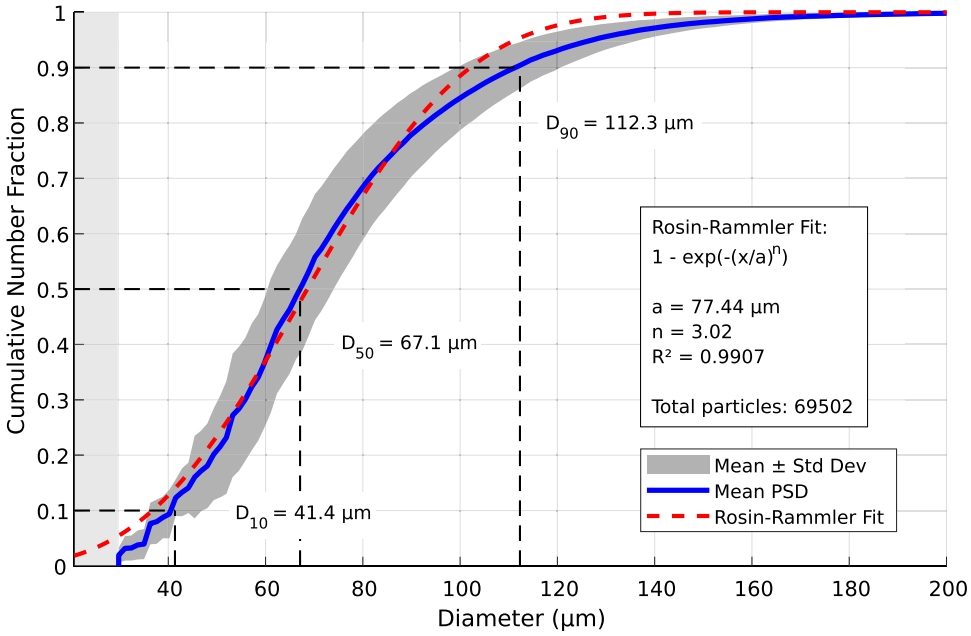

Fig. 7 Cumulative particle size distribution (PSD) by number from 70 000 tracked particles across nine cases. Mean PSD (blue line), inter-case variability (± 1σ band), and Rosin-Rammler fit (red dashed line) show consistent size distributions across operating conditions

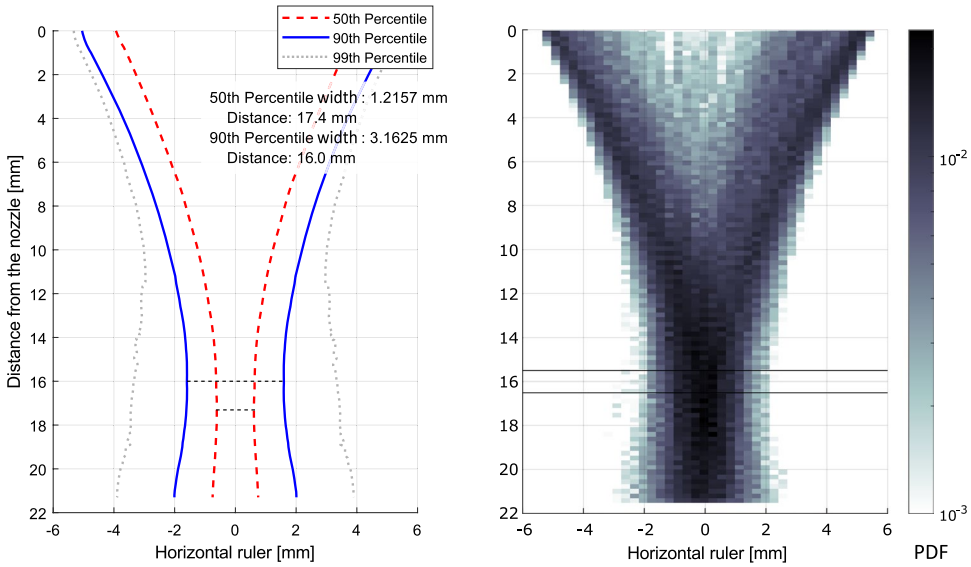

Fig. 8 Side view of the particle distribution analysis, averaged over the recording time (Case 5 in Table 2). Percentiles of the distribution are highlighted to determine the standoff distance. Darker colors indicate higher particle density. The horizontal lines denote a 1 mm thick slice around the standoff distance (Case 5 in Table 2)

More than 85% of the measured particles fall within the manufacturer's specified size range [20], validating the measurement technique.

3.2 Particle locations and standoff distance

The standoff distance, defined as the optimal distance between the nozzle and the workpiece, plays a critical role in the quality obtained in LMD. It ensures precise powder delivery to the melt pool, enabling uniform layer deposition and minimizing material waste. An incorrect standoff distance can lead to poor deposition quality, irregular layer thickness, and increased porosity.

The standoff distance is determined by analyzing the spatial distribution of the powder stream as it exits the nozzle. It is typically defined as the distance from the nozzle exit where the powder particles are most concentrated, corresponding to the minimum stream width containing a significant percentage (commonly 90%) of the particles. Accurate determination of this distance is essential for process optimization and achieving high-quality builds.

Figure 8 presents a side view of the particle distribution, averaged over the recorded time. The heatmap, normalized as a Probability Density Function (PDF), highlights the percentiles of the particle distribution. Darker colors indicate regions of higher particle density. The standoff distance, identified as the point of minimum stream width containing

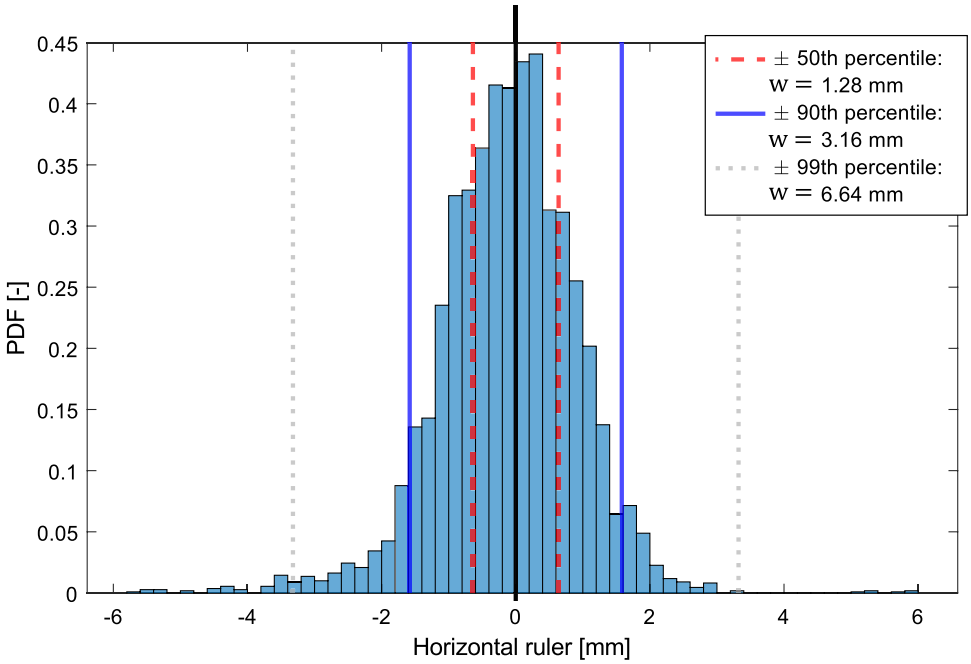

Fig. 9 Probability density function (PDF) of the particle distribution across the horizontal ruler at the standoff distance of 16.0 mm from the nozzle exit (Case 5 in Table 2). The red lines indicate the 50th percentile, the blue lines indicate the 90th percentile, and the gray lines indicate the 99th percentile (Case 5 in Table 2). The total stream width (w) is indicated in the legend

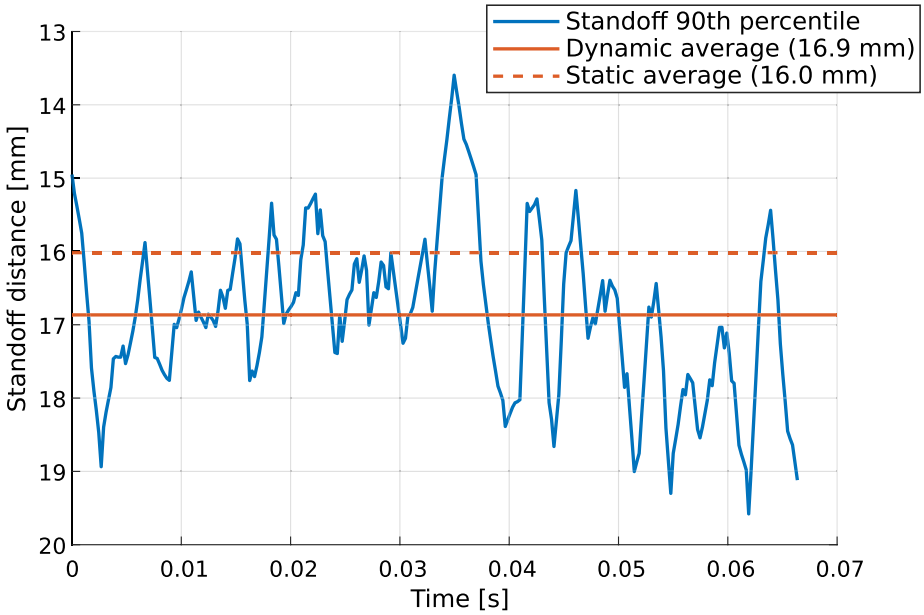

Fig. 10 Standoff distance variability, showing the average value and the oscillations over time (Case 5 in Table 2). Notice that average the value differs when calculated from the time evolution rather than the cumulated view

90% of the particles, is determined to be 16.0 mm from the nozzle exit. The two horizontal lines in the figure denote a 1 mm thick slice around this distance, representing the area of highest particle concentration.

Figure 9 shows the Probability Density Function (PDF) of the particle distribution across the horizontal ruler at the standoff distance of 16.0 mm. The red dashed lines indicate the 50th percentile (median) at ± 1.28 mm, representing the central concentration of particles. The blue lines indicate the 90th percentile at ± 3.16 mm, illustrating the region containing 90% of the particles. The gray dotted lines indicate the 99th percentile at ± 6.64 mm, highlighting the outer limits of particle dispersion.

The stream width, defined as the distance encompassing 90% of the particle distribution (between the blue lines in Fig. 9), directly influences the width of the material deposition trace. In this study, the stream width at the standoff distance is 3.16 mm.

The standoff distance oscillates around the average value of 16.0 mm by as much as ± 3 mm (or ≈ 19%), as can be observed in Fig. 10, which shows the average standoff distance over time, along with the time-dependent measurement filtered with a 2 ms moving average. Two average

standoff values are reported: the ”static average” (16.8 mm) is obtained by evaluating the 90th percentile envelope over all recorded particle positions simultaneously, as would result from a long-exposure measurement (Fig. 8), while the ”dynamic average” (16.0 mm) is the mean of the standoff distance over time and reflects the influence of instantaneous mass flow variations. In other words, the dynamic average effectively acts as a mass-flow-weighted mean, giving greater weight to moments with higher particle flux, which naturally leads to a slightly different average compared to the static envelope.

The standoff distance oscillates around an average value of $16.0\ \mathrm{mm}$, with excursions up to $\pm\ 3\ \mathrm{mm}$ $(\approx 19\%)$, as shown in Fig. 10, which presents the time-resolved standoff distance along with a 2 ms moving average. Two average values are reported: the “static average” (16.8 mm) is obtained by evaluating the 90th percentile envelope over all recorded particle positions simultaneously, as would result from a long-exposure measurement (Fig. 8), while the “dynamic average” (16.0 mm) is the mean of the standoff distance over time and reflects the influence of instantaneous mass flow variations. In other words, the dynamic average effectively acts as a mass-flow-weighted mean, giving greater weight to moments with higher particle flux, which naturally leads to a slightly lower average compared to the unweighted static envelope.

The oscillations can be attributed to the dynamic nature of the powder flow and the interaction between the powder and gas streams, which can lead to variations in particle concentration and distribution. This behavior is visible Fig. 11, which captures the width of the powder stream as 50th and 90th percentiles, in a way similar to Fig. 8, but resolved in time. A 1 mm band is represented around the optimal standoff distance, determined as the minimum width in the 90th percentile curves. The stream is captured for two time windows of 0.2 s, representing moments of minimum and maximum of the standoff distance. The image also represents the particles captured by the particle tracking method as dots. These snapshots illustrate the evolution of the stream shape over time, as it can be captured by using the presented method.

3.3 Particle velocities

The particle velocities are determined considering a $1\ \mathrm{mm}$ thick slice around the standoff distance estimated in Fig. 8. In this interval and over the whole recording time in case 5, the average velocity is $\mu_v = 1.989\ \mathrm{m/s}$, with a standard deviation of $\sigma_v = 0.220\ \mathrm{m/s}$. From Fig. 12, it is also evident that the velocity is fairly uniform over time.

There is a notable acceleration when particles exit the nozzle, and this is evident when selecting different locations

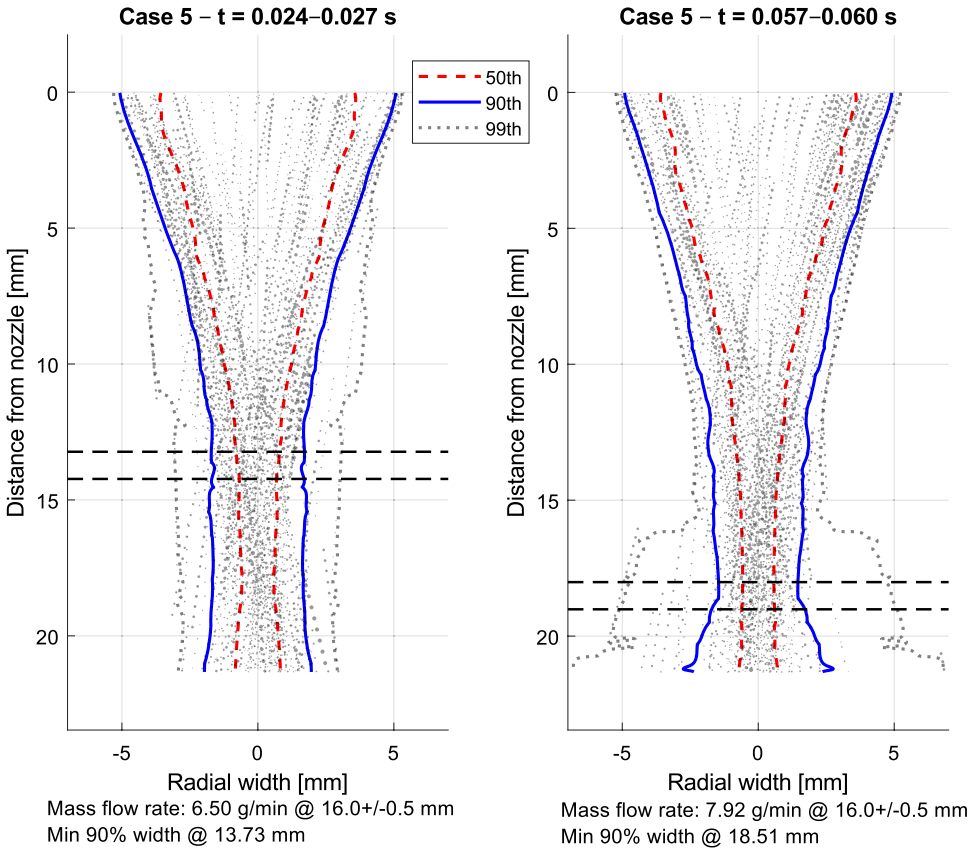

Fig. 11 Representation of the stream width at two different time windows, representing a minimum and maximum of the standoff distance of Fig. 10 (Case 5 in Table 2)

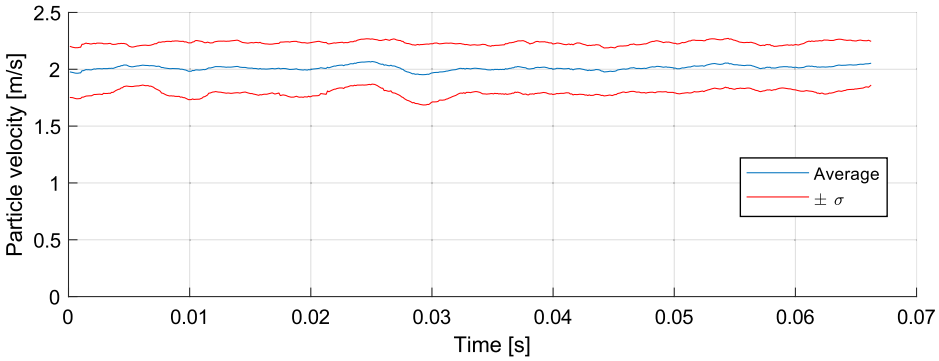

Fig. 12 Particle velocity over time, averaged in a 1 mm thick slice around the standoff distance 16.0 mm from the nozzle (Case 5 in Table 2)

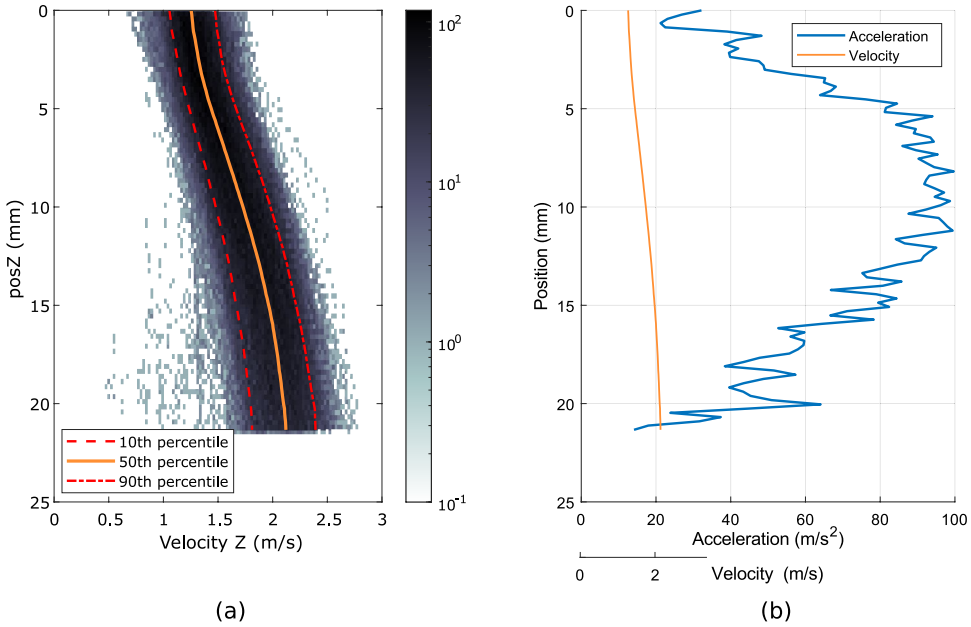

Fig. 13 **a** Particle vertical velocities heatmap along the stream, with percentiles. **b** Median acceleration. Case 5 in Table 2

along the stream. Figure 13a shows the median vertical particle velocities along the stream, and it is evident that they accelerate along the stream. Through a heatmap and the percentiles, the diagram also shows the distribution of the velocities.

The acceleration, given two velocities (v_1 and v_2) and two positions (z_1 and z_2), assuming constant acceleration, can be calculated using the kinematic equations:

$$v_2 = v_1 + at \tag{1}$$

$$\Delta z = v_1 t + \tfrac{1}{2} a t^2 \tag{2}$$

where:

- v_2 is the final velocity,
- v_1 is the initial velocity,
- a is the acceleration,
- $\Delta z = z_2 - z_1$ is the displacement,
- t is the time.

The Third kinematic equation relates these quantities from Eqs. (1) and (2), without involving time directly:

$$v_2^2 = v_1^2 + 2a(z_2 - z_1) \tag{3}$$

Rearranging Eq. 3 for acceleration (a):

$$a = \frac{v_2^2 - v_1^2}{2(z_2 - z_1)} \tag{4}$$

This results in the graph of Fig. 13b, where the average acceleration between the nozzle exit ($z_1 = 0$ mm) and a distance of $z_2 = 20$ mm is $\mu_a = 67.65$ m/s^2. Such a high acceleration value cannot be explained solely by gravity. A more likely explanation is that the particles interact with the lens shielding gas flow, which has a higher velocity than the carrier gas flow.

The nozzle geometry, shown in Fig. 2, consists of a central laser channel of diameter $D_s = 10$ mm. Surrounding it and separated by a sharp edge, the carrier gas transports

the particles through a ring-shaped channel with an internal diameter $D_{ci} \approx D_s$ and an external diameter $D_{ce} = 12$ mm.

A back-of-the-envelope calculation, using Bernoulli's principle and the flow conditions of case 5 from Table 2, gives the following estimates. The gas velocity at the center channel is:

$$u_s \approx \frac{Q_s}{A_s} = \frac{15 \text{ L/min}}{\frac{\pi}{4}(10^2) \text{ mm}^2} = 3.18 \text{ m/s}, \tag{5}$$

while in the annular section the velocity is:

$$u_c \approx \frac{Q_c}{A_c} = \frac{3 \text{ L/min}}{\frac{\pi}{4}(12^2 - 10^2) \text{ mm}^2} = 1.45 \text{ m/s}. \tag{6}$$

These values seem to explain most of the observed particle acceleration.

3.4 Mass flowrate estimation

The mass flowrate is evaluated at the standoff distance by means of a control-volume formulation consistent with the standard surface-based definition. In continuum form, the mass flowrate across a plane normal to the z direction is defined as

$$\dot{m} = \int_A \rho \, v_z \, dA, \tag{7}$$

where ρ is the mass density and v_z is the velocity component normal to the plane.

The same quantity can be equivalently expressed using a slab-shaped control volume of thickness Δz, bounded by two parallel planes normal to z. In the absence of mass accumulation within the slab, which is verified in the present steady-flow conditions, application of Reynolds' transport theorem yields

$$\dot{m} = \frac{1}{\Delta z} \int_V \rho \, v_z \, dV. \tag{8}$$

For a discrete particle system, the volume integral naturally reduces to a summation over the particles contained within the slab, leading to

$$\dot{m} = \frac{1}{\Delta z} \sum_{i=1}^{N} m_i \, v_{i,z}, \tag{9}$$

or, by expressing it as the individual contribution of each particle:

$$\dot{m} = \sum_{i=1}^{N} \dot{m}_i = \sum_{i=1}^{N} \frac{m_i \, v_{i,z}}{\Delta z}, \tag{10}$$

where m_i is the mass of particle i, $v_{i,z}$ is its velocity component along the z direction, and N is the number of particles contained in the control volume.

In this formulation, Δz does not represent an arbitrary physical length scale, but rather the thickness of the control volume used to perform a volume average of the mass flux. The value $\Delta z = 1$ mm was selected as it provides a representative sample of the particle flow at the standoff distance and is of the same order as the deposition thickness employed in the experimental setup.

Since particle positions and velocities are available only at discrete instants (frames), and explicit detection of plane-crossing events would introduce additional numerical noise, the control-volume formulation above was deemed the most appropriate estimator of the mass flowrate for the present data.

The average $\mu_{\dot{m}}$ and the standard deviation $\sigma_{\dot{m}}$ (sd) of the mass flowrate are defined as

$$\mu_{\dot{m}} = \frac{1}{T} \sum_{k=1}^{T} \dot{m}_k, \tag{11}$$

$$\sigma_{\dot{m}} = \sqrt{\frac{1}{T-1} \sum_{k=1}^{T} (\dot{m}_k - \mu_{\dot{m}})^2}, \tag{12}$$

where T is the total number of frames in the analyzed recording, and k denotes the index of an individual frame.

To evaluate the flow variability across the cases of Table 2, we use the coefficient of variation (CV) [19], also known as normalized root-mean-square deviation (NRMSD):

$$CV_{\dot{m}} = \frac{\sigma_{\dot{m}}}{\mu_{\dot{m}}}. \tag{13}$$

To reduce high-frequency fluctuations, a moving average filter is applied to the instantaneous mass flowrate. The smoothed value at frame k, $\dot{m}_{k,\text{smoothed}}$, is computed as

$$\dot{m}_{k,\text{smoothed}} = \frac{1}{w} \sum_{j=-\lfloor w/2 \rfloor}^{\lfloor w/2 \rfloor} \dot{m}_{k+j}, \tag{14}$$

where w is the window size expressed in number of frames.

3.5 Flow irregularities

Flow irregularities strongly affect the consistency and quality of material deposition in the LMD process. The temporal evolution of the mass flowrate was previously analyzed in [16], with a focus on pneumatic conveying in thin pipes.

Figure 14 shows the mass flowrate of the powder exiting the nozzle for Case 5, filtered with a moving average window of 2 ms. The average mass flowrate over the recording period was $\mu_{\dot{m}} = 6.910$ g/min, with a standard deviation of $\sigma_{\dot{m}} = 1.086$ g/min or $CV = 16\%$. The average is 56% above the setpoint. While oscillations in the mass flowrate are consistent with previous findings [16], the large deviation from the setpoint was unexpected. This discrepancy is most likely due to powder accumulation in the pipeline and insufficient equilibration time between successive recordings, which prevented the flow from reaching steady state. Although this issue is still under investigation, the method successfully achieved its purpose by enabling time-resolved monitoring of the mass flowrate and exposing a procedural limitation in the experimental setup.

These results point to an opportunity for process improvement: the proposed method can be implemented as a fast and reliable monitoring tool, enabling enhanced control of powder delivery in LMD.

3.6 Error analysis

Smaller particles are generally more difficult to track, which can lead to larger uncertainties in estimating both their velocity and mass flowrate. For this reason, we base our error analysis on particles with a small diameter. Since 80% of the particles have diameters between 41.4 and 112.3 μm (see Fig. 7), we now focus on particles with a diameter of 41.4 μm, as larger particles are expected to produce smaller relative errors.

For the error analysis, we also assume that the particles are spherical. While this assumption may not be exact (see Fig. 4), previous studies on similar gas-atomized steel powders indicate that deviations from sphericity do not significantly affect the results [11].

3.6.1 Velocity error

The velocity of each particle i is defined as

$$\vec{v}_i = \frac{\vec{x}_i(t) - \vec{x}_i(t - \Delta t)}{\Delta t}, \tag{15}$$

where $\vec{x}_i(t)$ is the two-dimensional position vector of particle i at time t, with components along the horizontal and vertical directions, and Δt is the time interval between consecutive frames.

When evaluating the powder flow, we consider only the vertical velocity component, orthogonal to the deposition plate:

$$v_i = \frac{z_i(t) - z_i(t - \Delta t)}{\Delta t}, \tag{16}$$

where $z_i(t)$ denotes the vertical position of particle i at time t.

We model the vertical position z_i, the time interval Δt, and the particle velocity v_i as the sum of their estimated value and an associated error term (Eq. 17)).

$$z_i = z_i^* \pm \varepsilon(z_i) \tag{17a}$$

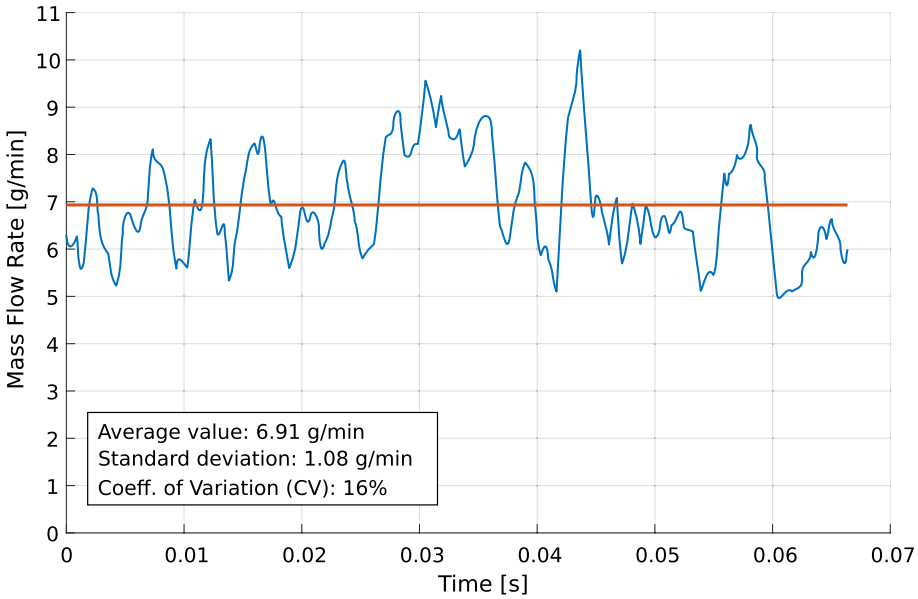

Fig. 14 Mass flowrate over time. Case 5 in Table 2

$$\Delta t = \Delta t^* \pm \varepsilon(\Delta t) \tag{17b}$$

$$v_i = v_i^* \pm \varepsilon(v_i) \tag{17c}$$

The superscript * indicates the estimated value, while $\varepsilon(\cdot)$ denotes the associated uncertainty, which we estimate according to the Guide to the Expression of Uncertainty in Measurement (GUM) [19].

To estimate the uncertainty associated with the particle positioning ($\varepsilon(z)$), we consider a representative configuration in which the particle is aligned with a line of the grid (Fig. 15). Since the pixel size is $15.6\,\mu\text{m}$, for particles of diameter $41.4\,\mu\text{m}$ this corresponds to roughly $41.4\,\mu\text{m}/15.6\,\mu\text{m} \simeq 2.65$ pixels, i.e. each particle spans about 2–3 pixels in the vertical direction.

The software automatically estimates the particle's position by identifying pixels occupied more than 50% by the particle, and then computing the barycenter of that pixel area. We examined different particle positions relative to the grid (Fig. 15) and evaluated the error obtained from computing the barycenter accordingly.

When the particle is vertically aligned with either the center or the edge of a pixel, its center matches the barycenter of the occupied pixels, producing no positional error (Fig. 15). In contrast, when the particle lies between a pixel's center and edge, the barycenter no longer coincides with the particle center, introducing a vertical position error of up to half a pixel, or $7.8\,\mu\text{m}$ (Fig. 15). Other configurations, such as horizontal shifts, could be considered, however, since we focus only on vertical displacements and velocity, we disregard those cases. Assuming a rectangular distribution of possible offsets [19], we calculate the uncertainty in vertical position as $\varepsilon(z) = 7.8\,\mu\text{m}/\sqrt{3} \simeq 4.5\,\mu\text{m}$.

We then estimate the uncertainty associated with the time interval Δt. Considering the frame rate of 4490 fps, the estimated time interval is $\Delta t^* = 1/4490\,\text{s} \simeq 0.22\,\text{ms}$, while the error in the frame timing $\varepsilon(\Delta t)$ is typically on the order of a few nanoseconds (www.aostechnologies.com). Assuming $\varepsilon(\Delta t) = 10\,\text{ns}$, we obtain that $\varepsilon(\Delta t)$ is lower than 0.01% of the estimated value.

We can now estimate the uncertainty associated with the particle velocity using the propagation of uncertainty law [19] (Eq. (18)):

$$\varepsilon(v_i) = \sqrt{\left(\frac{\partial v_i}{\partial z_i}\varepsilon(z_i)\right)^2 + \left(\frac{\partial v_i}{\partial \Delta t}\varepsilon(\Delta t)\right)^2} = \sqrt{\left(\frac{\varepsilon(z_i)}{\Delta t^*}\right)^2 + \left(-\frac{v_i^*}{\Delta t^*}\varepsilon(\Delta t)\right)^2} \tag{18}$$

This uncertainty depends on the particle *i*, however, as we are focusing on the worst-case scenario of small particles, we neglect the particle dependence and rewrite the uncertainty related to the particle velocity as in Eq. (19):

$$\varepsilon(v) = \sqrt{\left(\frac{\varepsilon(z)}{\Delta t^*}\right)^2 + \left(-\frac{v^*}{\Delta t^*}\varepsilon(\Delta t)\right)^2}, \tag{19}$$

where $\varepsilon(z)$ and $\varepsilon(\Delta t)$ are the uncertainties previously estimated, and v^* is the estimated particle velocity. For small particles, we consider the average velocity at the standoff distance, $v^* \simeq 2\,\text{m/s}$ (see Fig. 12). Substituting the numerical values into Eq. (19), we get $\varepsilon(v) \simeq 2 \cdot 10^{-2}\,\text{m/s}$ which is approximately 1% of v^*.

3.6.2 Mass flowrate error

The calculation of the mass flowrate relies on the particle's mass, its velocity, and the thickness of each recorded slice (Eq. (10)). Assuming spherical particles, the mass flowrate for particle *i* is given by Eq. (20):

$$\dot{m}_i = \frac{\rho\,\frac{4}{3}\pi r_i^3 v_i}{\Delta z}, \tag{20}$$

where r_i is the radius of the particle, v_i its velocity, ρ the particle density, and Δz the thickness of the measurement slice. We model each of these quantities as the sum of their estimated value and an associated error term (Eq. (21)).

$$\rho = \rho^* \pm \varepsilon(\rho) \tag{21a}$$

$$r_i = r_i^* \pm \varepsilon(r_i) \tag{21b}$$

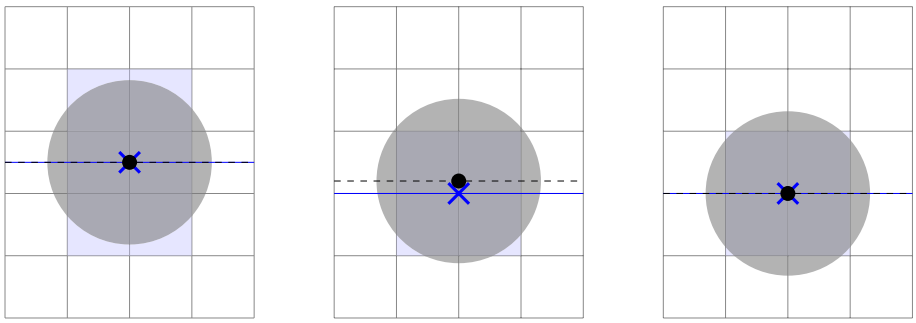

Fig. 15 Positioning of the particle on the pixel grid to estimate position uncertainty. The gray circle represents the particle, with its center marked by a black point. Pixels occupied more than 50% by the particle are shown in purple, and the barycenter of these pixels is indicated by the blue X

$$v_i = v_i^* \pm \varepsilon(v_i) \tag{21c}$$

$$\Delta z = \Delta z^* \pm \varepsilon(\Delta z) \tag{21d}$$

This means that any uncertainty in these quantities will propagate to the particle mass flowrate $\dot{m}_i$, and in particular to its uncertainty $\varepsilon(\dot{m}_i)$ (Eq. (22)).

$$\dot{m}_i = \dot{m}_i^* \pm \varepsilon(\dot{m}_i) \tag{22}$$

We estimate this uncertainty by applying the propagation of uncertainty law [19], leading to Eq. (23).

$$\begin{aligned}\varepsilon(\dot{m}_i) &= \sqrt{\left(\frac{\partial \dot{m}_i}{\partial \rho}\varepsilon(\rho)\right)^2 + \left(\frac{\partial \dot{m}_i}{\partial r_i}\varepsilon(r_i)\right)^2 + \left(\frac{\partial \dot{m}_i}{\partial v_i}\varepsilon(v_i)\right)^2 + \left(\frac{\partial \dot{m}_i}{\partial \Delta z}\varepsilon(\Delta z)\right)^2} \\ &= \sqrt{\left(\frac{\dot{m}_i^*}{\rho^*}\varepsilon(\rho)\right)^2 + \left(\frac{3\dot{m}_i^*}{r_i^*}\varepsilon(r_i)\right)^2 + \left(\frac{\dot{m}_i^*}{v_i^*}\varepsilon(v_i)\right)^2 + \left(\frac{\dot{m}_i^*}{\Delta z^*}\varepsilon(\Delta z)\right)^2}\end{aligned} \tag{23}$$

As before, this uncertainty depends on the particle *i*, however, as we are focusing on the case of small particles, we neglect the particle dependence, and rewrite the uncertainty related to the particle mass flowrate (Eq. (24)):

$$\varepsilon(\dot{m}) = \sqrt{\left(\frac{\dot{m}^*}{\rho^*}\varepsilon(\rho)\right)^2 + \left(\frac{3\dot{m}^*}{r^*}\varepsilon(r)\right)^2 + \left(\frac{\dot{m}^*}{v^*}\varepsilon(v)\right)^2 + \left(\frac{\dot{m}^*}{\Delta z^*}\varepsilon(\Delta z)\right)^2} \tag{24}$$

To estimate the uncertainty $\varepsilon(\dot{m})$, we evaluate the contributions associated with each quantity appearing in Eq. (24). We begin by considering the uncertainty in the mass density, $\varepsilon(\rho)$. Given the well-characterized material properties, the uncertainty in ρ is negligible compared to its estimated value ρ^* [11]. Consequently, the contribution of $\varepsilon(\rho)$ to the overall mass flowrate uncertainty is neglected.

We next consider the uncertainty associated with the slice thickness. A misalignment between the slice and the pixel grid may introduce an error of at most one pixel, accounting for the combined offset at the top and bottom of the slice (see Fig. 15). Since each pixel corresponds to $15.6\,\mu\text{m}$, and by analogy with the uncertainty in the vertical position, the uncertainty in the slice thickness is estimated as $\varepsilon(\Delta z) = (15.6\,\mu\text{m}/2)/\sqrt{3} \simeq 4.5\,\mu\text{m}$.

We now turn to estimating the uncertainty in the particle radius, $\varepsilon(r)$. This requires understanding how the software estimates r^*. The software first determines the number of pixels occupied by each particle. Assuming that this pixel area corresponds to the particle's projected area, the radius is then computed using the relation $A^* = \pi(r^*)^2$.

For small particles with radius $r^* = 20.70\,\mu\text{m}$, the projected area is approximately $A^* \simeq 1346\,\mu\text{m}^2$, which corresponds to about 5.5 pixels. However, in practice, the number of detected pixels may vary depending on the particle's position with respect to the pixel grid (Fig. 16). To investigate this, we ran a Monte Carlo simulation to estimate the number of pixels occupied by a particle and hence its radius (supplementary file). The results show that the most probable values are 6 and 5 pixels (see Fig. 17), consistent with the theoretical estimate of 5.5 pixels. In compliance with the GUM [19], we estimate the uncertainty related to the particle radius from the Monte Carlo standard deviation, obtaining $\varepsilon(r) = 1.7\,\mu\text{m}$, which is roughly 8% of the estimated particle radius.

Substituting this and the previous estimates into Eq. (24), the resulting mass flowrate is $0.0356 \pm 0.0087\,\text{g/min}$, meaning that the uncertainty $\varepsilon(\dot{m}_i)$ can reach up to 24% of its estimated value (supplementary file). While such a deviation is significant, it represents a worst-case scenario for small particles. When considering larger, and thus more prevalent, particles, the relative uncertainty decreases. For instance, for particles with radii of $33.55\,\mu\text{m}$ and $56.15\,\mu\text{m}$ (half of D_{50} and D_{90} respectively, Fig. 7), the uncertainties in mass flowrate reduce to approximately 8% and 3.5% of their estimated values, respectively (supplementary file).

The analysis presented so far provides an estimate of the uncertainty in the mass flowrate of a single particle. We

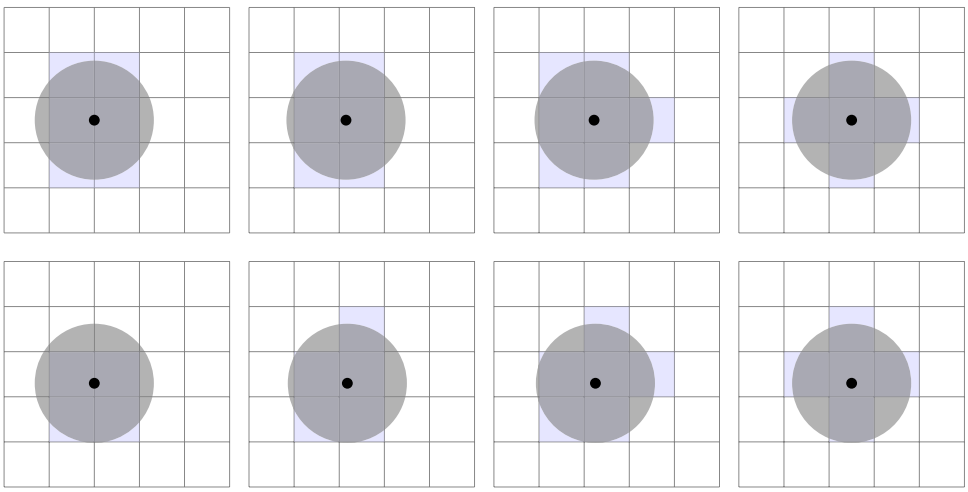

Fig. 16 Positioning of the particle on the pixel grid to estimate radius uncertainty. The gray circle represents the particle, with its center marked by a black point. Pixels occupied by more than 50% of the particle are shown in purple

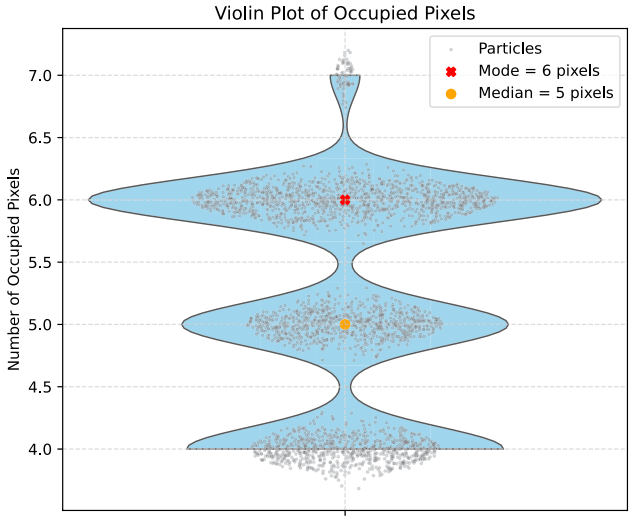

Fig. 17 Estimating the number of pixels occupied by a particle via Monte Carlo simulation. Violin plot (in cyan) of the number of pixels occupied by 3000 particles (black dots) of radius 20.7 μm on a grid of pixel size 15.6 μm

now extend this approach to compute the total mass flowrate of all particles detected within a 1 mm slice at the average standoff distance (see Sect. 3.2) during a single time frame k of duration 0.22 ms.

Let N denote the number of particles detected in this time interval. The mass flowrate contribution of the i-th particle, $\dot{m}_i$, is treated as a random variable and decomposed into an estimated value and an uncertainty term $\varepsilon(\dot{m}_i)$ (see Eq. 23). We assume that $\varepsilon(\dot{m}_i)$ has zero mean and variance σ^2.

Since the true variance is unknown, we approximate the standard deviation σ using the uncertainty $\varepsilon(\dot{m})$ previously computed for small particles. Under this assumption, the total mass flowrate for time frame k is obtained by summing the individual particle contributions, yielding

$$\dot{m}_k = \sum_{i=1}^{N} \dot{m}_i = \sum_{i=1}^{N} \dot{m}_i^* \pm \varepsilon(\dot{m}_i), \tag{25}$$

with its variance and standard deviation bounded by

$$\mathrm{Var}(\dot{m}_k) \leq N\sigma^2 \leq N(\varepsilon(\dot{m}))^2, \tag{26}$$

$$\mathrm{sd}(\dot{m}_k) \leq \sqrt{N}\,\varepsilon(\dot{m}). \tag{27}$$

On the other hand, because $\varepsilon(\dot{m}_i)$ has zero mean, the expected value of the total mass flowrate is

$$\mathbb{E}[\dot{m}_k] = N\,\mathbb{E}[\dot{m}_i]. \tag{28}$$

Hence, the relative standard deviation of the total mass flowrate is bounded by

$$\frac{\mathrm{sd}(\dot{m}_k)}{\mathbb{E}[\dot{m}_k]} \leq \frac{\sqrt{N}\,\varepsilon(\dot{m})}{N\,\mathbb{E}[\dot{m}_i]} = \frac{\varepsilon(\dot{m})}{\sqrt{N}\,\mathbb{E}[\dot{m}_i]}. \tag{29}$$

This implies that as the number of particles N increases, the relative error decreases proportionally to $1/\sqrt{N}$. Considering an average of $N \simeq 17$ particles recorded during one time frame, we obtain a reduction factor of about 1/4.1. Thus, if the relative error for a single particle mass flowrate is around 24% of the estimated value, the relative error for the total mass flowrate lowers to $24\%/4.1 \simeq 5.8\%$. This estimate would further decrease when using the moving average window of 2 ms, during which an average of $N \simeq 150$ particles is recorded, resulting in an error of 2%. We note that this $1/\sqrt{N}$ reduction assumes independent, zero-mean errors across particles; any systematic segmentation bias would not average out and would make these bounds optimistic.

3.7 Comparative analysis

Table 3 presents the mass flowrate and particle velocity parameters for each case in the experiment, as calculated

Table 3 Mass flowrate and particle velocity measurements for each case in the experiment, as calculated in Sect. 3.4, at the ideal average standoff distance determined with the 90th-percentile profile

Case	Mass flowrate		Velocity		90th-percentile profile	
	$\mu_{\dot{m}}$ [g/min]	$CV_{\dot{m}}$ [%]	μ_v [m/s]	CV_v [%]	Width	Standoff
1	2.53	22.63	1.433	8.32	2.76	14.7
2	1.62	26.21	1.490	9.19	2.80	12.9
3	1.70	19.40	1.970	11.17	2.96	12.0
4	4.48	15.83	1.451	9.99	2.66	13.8
5	6.91	15.69	1.989	11.07	3.16	16.0
6	7.31	14.28	1.996	11.18	3.27	15.3
7	3.60	21.81	2.016	10.70	3.22	18.0
8	6.24	16.92	1.577	9.68	3.11	13.6
9	5.69	19.48	2.082	10.94	3.25	12.6

The case numbers reference the parameters in Table 2

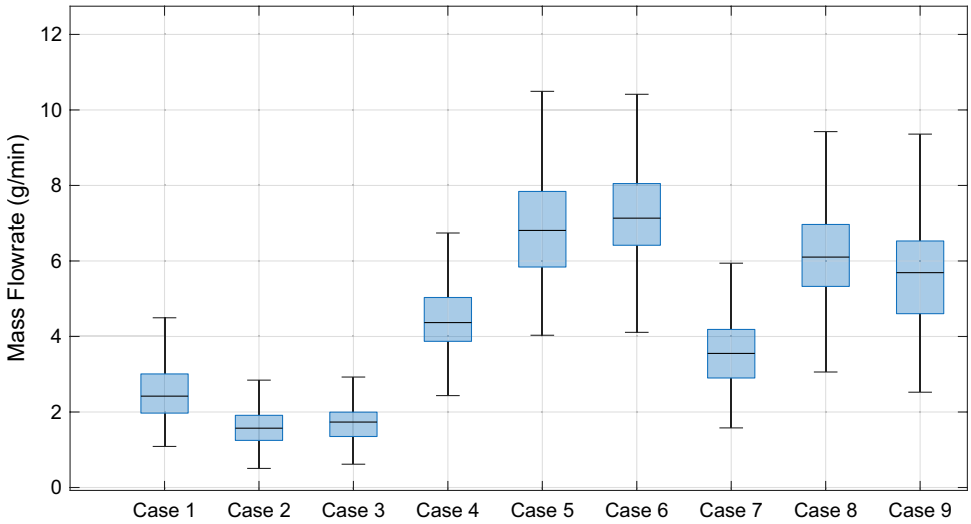

Fig. 18 Comparative boxplots of measured mass flowrate by case. Boxes show IQR with median; whiskers extend to $1.5\times$ IQR; markers denote mean. Cases are grouped by nominal mass-flow setpoint (1–3, 4–6, 7–9); case numbers and parameter levels per Table 2

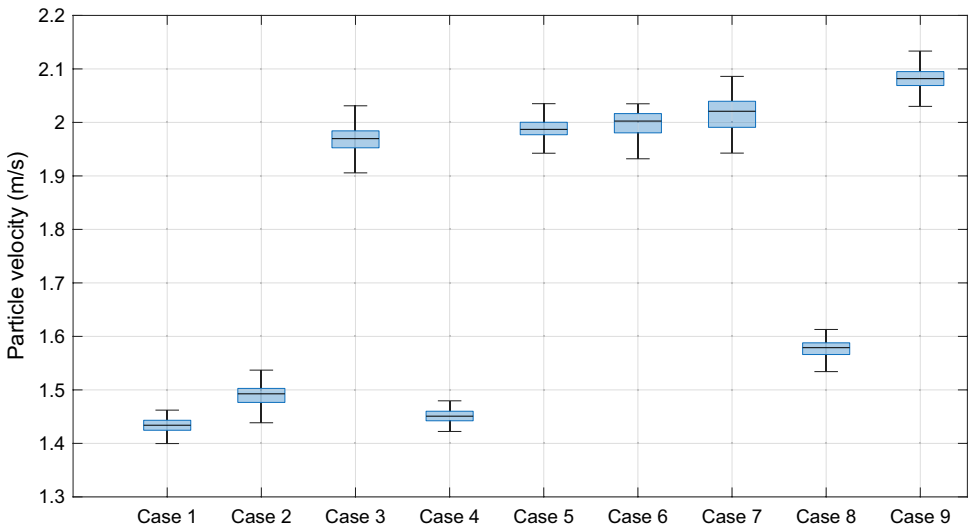

Fig. 19 Comparative boxplots of measured particle velocity by case. Boxes show IQR with median; whiskers extend to $1.5\times$ IQR; markers denote mean. Case numbers and parameter levels per Table 2

in Sect. 3.4. The case numbers reference the parameters in Table 2.

To interpret the measured mass flowrate signals, Fig. 18 summarizes the case-wise distributions (median, interquartile range, whiskers); cases are indicated per Table 2; note that the cases can be grouped by nominal mass-flow setpoint (1–3, 4–6, 7–9).

Within-group trends point to a carrier-gas effect at the medium and high setpoints: in groups 4–6 and 7–9, the lowest carrier-gas level (Cases 4 and 7) yields markedly lower achieved mass flow than the other two settings (Table 3), indicating that carrier gas substantially assists powder transport. In the low-setpoint group (1–3), case 1 exceeds cases 2–3. The carrier gas shows an important role in the powder delivery, that in this instance has an opposite effect between the low and high setpoints, but more work is needed to clarify this aspect.

Across all cases, the coefficient of variation of the mass-flow signal (CV in Table 3) ranges from roughly 14–26%, with higher variability in groups 1–3 and 7–9 than in 4–6. This indicates limited feeder resolution and/or intermittent feeding; a finer adjustment or closed-loop regulation would likely reduce both bias and dispersion relative to the nominal levels in Table 2.

Particle velocities are bimodal rather than uniform (Fig. 19): a low-velocity mode around 1.5 m/s (cases 1, 2, 4, 8) and a high-velocity mode around 2.0–2.1 m/s (cases 3, 5, 6, 7, 9). The between-mode gap ($\sim$0.5 m/s) exceeds the within-case variability (standard deviation $\sim$0.12–0.23 m/s; Table 3), indicating two operating regimes. This bimodality does not map one-to-one to the nominal mass-flow setpoints (1–3, 4–6, 7–9), but it aligns with gas settings: the highest shielding-gas level (cases 3, 5, 7; Table 2) appears in the high-velocity mode, whereas the lowest carrier-gas setting within groups coincides with reduced velocity in two instances (cases 4 and 8). Overall, velocities are less sensitive to nominal feed than to gas conditions and do not track achieved mass flow monotonically.

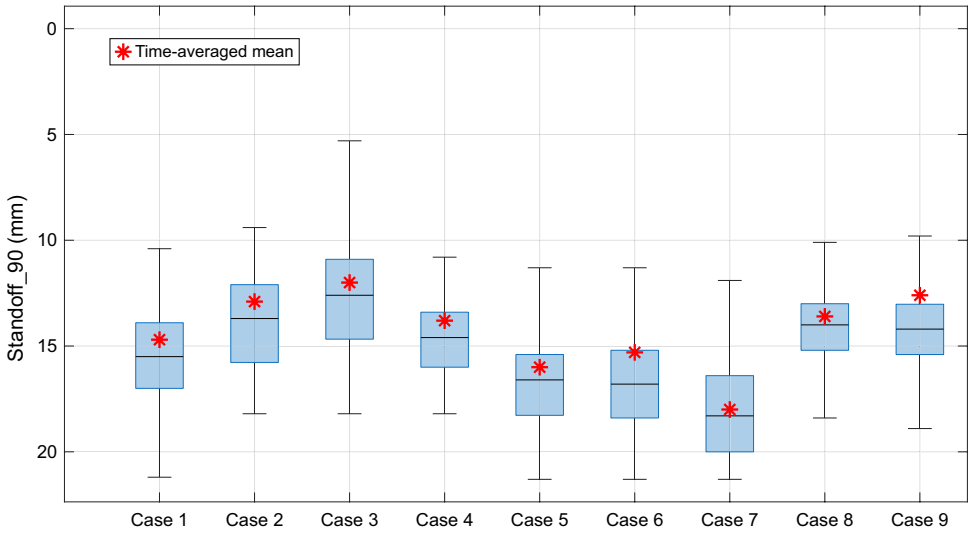

Fig. 20 Distribution of standoff distance over time for the 90th-percentile profile. The time-averaged mean matches Table 3. Case numbers and parameter levels per Table 2

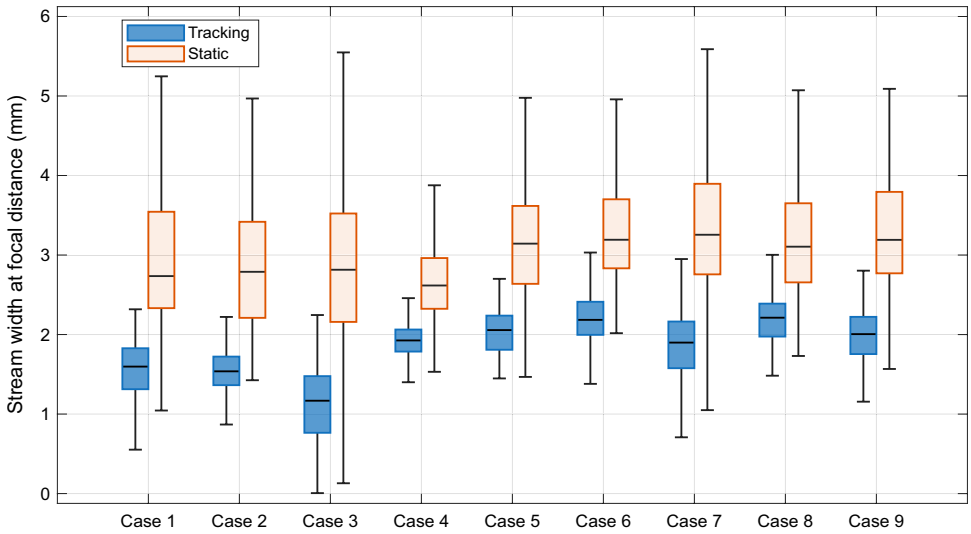

Fig. 21 Distribution of the minimum stream width over time for the 90th-percentile profile, either tracking the optimal standoff distance or keeping the distance static. The static condition matches the mean values reported in Table 3. Case numbers and parameter levels per Table 2

Figure 20 shows the distribution of standoff distance over time for each case. The time-averaged mean is the value reported in Table 3 for the 90th-percentile profile. The median is close to the time-averaged mean, and the standoff oscillates with a maximum standard deviation of about ± 2 mm for case 3.

The effect of standoff distance on the minimum stream width is shown in Fig. 21, which presents two box plots: the ”static condition” (stream width evaluated at the time-averaged standoff distance from the nozzle; see Fig. 20) and ”tracking” (stream width evaluated at the instantaneous minimum, i.e. tracking the optimal standoff distance). As expected, the width variability determined by following the minimum width over time is much smaller than the width determined while keeping the observation at the same standoff distance across the recording.

Case 3 presents the highest width fluctuations, including instants with no powder particles within the region of interest of thickness 1 mm around the ideal standoff distance, which is also the shortest. Other cases still exhibit notable variability in minimum width, a factor that can affect deposited trace geometry and increase the fraction of powder not captured in the molten pool. Overall, Case 4 is the one that exhibits the mass flowrate that is closest to the setpoint (4.5 g/min), with a low variability (15.8 %). Its powder velocity is in the low side (1.468 m/s), while the standoff distance and stream width are slightly more stable than the other cases.

4 Conclusion

This work demonstrates that high-speed imaging combined with particle tracking provides a practical, non-intrusive means to characterize powder flow in Laser Metal Deposition. By exploiting back illumination and short exposure times we obtained clear particle images that allowed reliable segmentation and sizing; the resulting size distributions

agreed well with the manufacturer's specification, lending confidence to the measurements. The method produced time-resolved maps of the stream geometry and kinematics: for our nozzle and test conditions Case 5 is representative of typical operating settings, with an optimal standoff of $16.0\ \mathrm{mm}$ (90th-percentile profile) and a stream width of $3.16\ \mathrm{mm}$ at that position. It is possible to analyze particle kinematics along the stream, which showed an average speed near $2.01\ \mathrm{m/s}$ and accelerations on the order of $68\ \mathrm{m/s^2}$.

Beyond these point estimates, the optical diagnostics revealed two practical phenomena that have direct implications for deposition quality. First, the measured mass flow can differ substantially from the nominal feed setting: Case 5, for example, delivered a mean flow of $6.91\ \mathrm{g/min}$ while the controller was set to $4.5\ \mathrm{g/min}$, and exhibited 16% short-time irregularity (CV) when smoothed with a 2 ms window. Second, the standoff distance oscillated significantly around its mean (recorded variations up to about $\pm 19\%$). For all considered cases, evaluating stream width while "tracking" the instantaneous optimal standoff produced markedly narrower minima and reduced variability compared with using a fixed, time-averaged standoff. Real-time tracking of the optimal standoff could therefore preserve narrower streams and reduce powder loss, either via closed-loop trajectory control or, in future work, by mitigating standoff oscillations through powder-delivery improvements.

The study's uncertainty analysis shows that, although individual-particle mass estimates are sensitive to segmentation and pixelation (leading to larger relative errors for the smallest particles), averaging over many particles reduces the uncertainty on the total mass flowrate to the percent level under the tested conditions (roughly 0.7–1.1% with the 2 ms window). This reduction assumes independent, zero-mean errors across particles; any systematic segmentation bias, overlapping particles, or correlated errors would degrade these optimistic bounds and require additional calibration.

Limitations of this work include its restriction to a single nozzle geometry, one powder batch and a finite Taguchi array of operating points; these choices were adequate to demonstrate the method but limit immediate generalisation. Future work should therefore pursue two parallel strands: improving the sensing and analysis (for example, better optics, sub-pixel sizing, multi-angle imaging and in-situ calibration against gravimetric measurements) to lower systematic errors, and translating the diagnostics into control or hardware changes (closed-loop standoff control, better feeder calibration, active metering) to quantify achievable gains in material capture and trace fidelity. Finally, linking the optical metrics reported here to metallurgical outcomes (melt-pool capture, track geometry and microstructure) will be necessary to close the loop between powder-flow diagnostics and part quality.

Overall, the imaging and particle-tracking workflow introduced here offers a high-resolution tool for diagnosing powder-delivery performance in LMD: it exposes both steady offsets and dynamic variability that are otherwise not observed, and it points to concrete routes–through measurement, calibration, and control–to reduce powder loss and improve additive-manufacturing consistency.

Supplementary Information The online version contains supplementary material available at https://doi.org/10.1007/s40964-026-01600-3.

Author contributions L.P. conceived and designed the study, developed the methodology and software, performed the experiment, curated and visualized the data, and wrote the original draft. J.I.A.A. contributed to the investigation and data curation, and participated in reviewing and editing the manuscript. G.B. contributed to data curation and co-wrote the original draft. A.La. provided resources and supervision. B.A. and A.Lo. supervised the project, acquired funding, and contributed to reviewing and editing the manuscript.

Funding Open Access funding provided thanks to the CRUE-CSIC agreement with Springer Nature.

Data availability The data are available upon request to the authors.

Declarations

Conflict of interest The authors declare no conflict of interest.

References

1. Dadbakhsh S, Hao L, Kong C (2010) Surface finish improvement of LMD samples using laser polishing. Virtual Phys Prototyp 5:215–221. https://doi.org/10.1080/17452759.2010.528180
2. Freeman FSHB, Thomas B, Chechik L, Todd I (2022) Multi-faceted monitoring of powder flow rate variability in directed energy deposition. Addit Manuf Lett 2:100024. https://doi.org/10.1016/j.addlet.2021.100024
3. Tabernero I, Lamikiz A, Ukar E, Lacalle LN, Angulo C, Urbikain G (2010) Numerical simulation and experimental validation of powder flux distribution in coaxial laser cladding. J Mater

Process Technol 210(15):2125–2134. https://doi.org/10.1016/j.jmatprotec.2010.07.036
4. Ostolaza M, Urresti A, Arrizubieta JI, Lamikiz A, Ortiz M (2022) Cfd simulation for the modelling of the powder flow on continuous coaxial nozzles in the laser ded process. Procedia CIRP 111, 282–286 https://doi.org/10.1016/j.procir.2022.08.022. 12th CIRP conference on photonic technologies [LANE 2022]
5. López-Martínez A, Ibarra-Medina J, García-Moreno A-I, Piedra S, Llano Vizcaya L, Martínez-Franco E, Megahed M (2023) Modeling and comparison of the powder flow dynamics for tilted annular and discrete-outlet nozzles in laser directed energy deposition. J Manuf Process 99: 687–704 https://doi.org/10.1016/j.jmapro.2023.05.039
6. Gao J, Wu C, Liang X, Hao Y, Zhao K (2020) Numerical simulation and experimental investigation of the influence of process parameters on gas-powder flow in laser metal deposition. Opt Laser Technol 125:106009. https://doi.org/10.1016/j.optlastec.2019.106009
7. Guner A, Bidare P, Jimenez A, Dimov S, Essa K (2022) Nozzle designs in powder-based direct laser deposition: a review. Int J Precis Eng Manuf 23(9):1077–1094. https://doi.org/10.1007/s12541-022-00688-1
8. Piscopo G, Atzeni E, Saboori A, Salmi A (2022) An overview of the process mechanisms in the laser powder directed energy deposition. Appl Sci 13(1):117. https://doi.org/10.3390/app13010117
9. Metco Joining & Cladding: Twin 150-LC Powder Feeder (2024). https://www.metcojoiningcladding.com/en/products-services/twin150/ Accessed 2024–07-03
10. Metco O (2023) MetcoAdd 316L-D . https://mymetco-europe.oerlikon.com/en-us/product/metcoadd316ld
11. Nan W, Pasha M, Bonakdar T, Lopez A, Zafar U, Nadimi S, Ghadiri M (2018) Jamming during particle spreading in additive manufacturing. Powder Technol 338:253–262. https://doi.org/10.1016/j.powtec.2018.07.030
12. Odum K, Soshi M, Yamazaki K (2022) Measurement and analysis of impact dynamics suitable for modelling pneumatic transport of metallic powder flow through a directed energy deposition nozzle. Adv Powder Technol 33(3):103515. https://doi.org/10.1016/j.apt.2022.103515 Accessed 2022-05-17
13. García-Moreno A-I, Alvarado-Orozco J-M, Ibarra-Medina J, López-Martínez A, Martínez-Franco E (2021) A new PIV method to measure powder flow velocity in laser metal deposition: an Eulerian-based approach. Int J Adv Manuf Technol 117(5–6):1825–1841. https://doi.org/10.1007/s00170-021-07730-y
14. Schindelin J, Arganda-Carreras I, Frise E, Kaynig V, Longair M, Pietzsch T, Preibisch S, Rueden C, Saalfeld S, Schmid B, Tinevez J-Y, White DJ, Hartenstein V, Eliceiri K, Tomancak P, Cardona A (2012) Fiji: an open-source platform for biological-image analysis. Nat Methods 9(7):676–682. https://doi.org/10.1038/nmeth.2019. Accessed 2023-01-19
15. Tinevez J-Y, Perry N, Schindelin J, Hoopes GM, Reynolds GD, Laplantine E, Bednarek SY, Shorte SL, Eliceiri KW (2017) Trackmate: an open and extensible platform for single-particle tracking. Methods 115:80–90. https://doi.org/10.1016/j.ymeth.2016.09.016
16. Pedrolli L, Fraccarollo L, Achiaga B, Lopez A (2024) Optical particle tracking in the pneumatic conveying of metal powders through a thin capillary pipe. Technologies 12(10):191. https://doi.org/10.3390/technologies12100191
17. Ferreira E, Dal M, Colin C, Marion G, Gorny C, Courapied D, Guy J, Peyre P (2020) Experimental and numerical analysis of gas/powder flow for different LMD nozzles. Metals 10(5):667. https://doi.org/10.3390/met10050667. Accessed 2022-03-11
18. Nadimi S, Angelidakis V, Maramizonouz S, Zhang C (2025) Automated dynamic image analysis for particle size and shape classification in three dimensions. Powder Technol 458:120973. https://doi.org/10.1016/j.powtec.2025.120973
19. Joint Committee for Guides in Metrology (JCGM): Evaluation of Measurement Data–Guide to the Expression of Uncertainty in Measurement. Bureau International des Poids et Mesures (BIPM), (2008). Bureau International des Poids et Mesures (BIPM). JCGM 100:2008, with https://doi.org/10.59161/JCGM100-2008E
20. Oerlikon: Datasheet of gas-atomized powder MetcoAdd 316L-D (2024). https://mymetco-europe.oerlikon.com/en-us/product/metcoadd316ld